

**Real-time monitoring of electrochemically induced calcium carbonate depositions  
Kinetics and mechanisms**

Liu, Zilong; Onay, Hayati; Guo, Fengzhi; Lv, Qichao; Sudhölter, Ernst J.R.

**DOI**

[10.1016/j.electacta.2021.137719](https://doi.org/10.1016/j.electacta.2021.137719)

**Publication date**

2021

**Document Version**

Final published version

**Published in**

Electrochimica Acta

**Citation (APA)**

Liu, Z., Onay, H., Guo, F., Lv, Q., & Sudhölter, E. J. R. (2021). Real-time monitoring of electrochemically induced calcium carbonate depositions: Kinetics and mechanisms. *Electrochimica Acta*, 370, Article 137719. <https://doi.org/10.1016/j.electacta.2021.137719>

**Important note**

To cite this publication, please use the final published version (if applicable).  
Please check the document version above.

**Copyright**

Other than for strictly personal use, it is not permitted to download, forward or distribute the text or part of it, without the consent of the author(s) and/or copyright holder(s), unless the work is under an open content license such as Creative Commons.

**Takedown policy**

Please contact us and provide details if you believe this document breaches copyrights.  
We will remove access to the work immediately and investigate your claim.



ELSEVIER

Contents lists available at ScienceDirect

Electrochimica Acta

journal homepage: [www.elsevier.com/locate/electacta](http://www.elsevier.com/locate/electacta)

# Real-time monitoring of electrochemically induced calcium carbonate depositions: Kinetics and mechanisms



Zilong Liu<sup>a,b,\*</sup>, Hayati Onay<sup>b</sup>, Fengzhi Guo<sup>a</sup>, Qichao Lv<sup>c,\*\*</sup>, Ernst J.R. Sudhölter<sup>b</sup>

<sup>a</sup> Beijing Key Laboratory of Optical Detection Technology for Oil and Gas, College of Science, China University of Petroleum (Beijing), Beijing 102249, China

<sup>b</sup> Organic Materials & Interfaces, Department of Chemical Engineering, Faculty of Applied Sciences, Delft University of Technology, Van der Maasweg 9, 2629 HZ Delft, the Netherlands

<sup>c</sup> Unconventional Petroleum Research Institute, China University of Petroleum (Beijing), Beijing 102249, China

## ARTICLE INFO

### Article history:

Received 24 October 2020

Revised 21 December 2020

Accepted 2 January 2021

Available online 6 January 2021

### Keywords:

Electrochemically assisted deposition

Calcium carbonate precipitation

Magnesium ions

EQCM-D

Scaling

## ABSTRACT

Calcium carbonate ( $\text{CaCO}_3$ ) deposition plays a significant role in processes such as scale formation in power plants and in oil or gas production wells. The development of appropriate methods based on well suitable *in situ* sensors is important to evaluate and predict the deposition process. In this study, a combination of electrochemical techniques and quartz crystal microbalance with dissipation monitoring (QCM-D) in one analysis setup (EQCM-D) was used for the first time to monitor the  $\text{CaCO}_3$  deposition in real time and provide kinetic details of the  $\text{CaCO}_3$  deposition process. Through recording the frequency change of quartz crystal sensors, it allows us to perform a quantitative analysis of the morphology, coverage, deposition rate, and mass changes with nanogram sensitivity. By varying the applied voltage, it was found that a lower applied voltage resulted in more deposition of  $\text{CaCO}_3$  mass and increase of the thickness of the deposited layer. Under the absence of flow, the  $\text{CaCO}_3$  growth rate switched from accelerating to decelerating and this point is characterized by an inflection point (IP). A lower applied voltage resulted in a lower IP. Increasing  $\text{Ca}^{2+}$  and  $\text{HCO}_3^-$  concentrations, both the deposited amount of  $\text{CaCO}_3$  mass and coating thickness increased correspondingly. With the addition of 50 mM  $\text{Mg}^{2+}$ , a reduction in the deposition rate of  $\text{CaCO}_3$  as high as 73% was achieved. The higher the  $\text{Mg}^{2+}$  concentration, the larger the deposition rate reduction, which was attributed to the incorporation of  $\text{Mg}^{2+}$  into the growing  $\text{CaCO}_3$  mineral, resulting in the reduction of growth sites (inhibiting effect). The obtained results contribute to a better understanding of electrochemically induced  $\text{CaCO}_3$  deposition and provide valuable insights into the determination of optimal precipitation parameters, with the aim to optimize industry scaling and anti-scaling processes.

© 2021 Published by Elsevier Ltd.

## 1. Introduction

The formation of calcium carbonate ( $\text{CaCO}_3$ ) in aqueous systems has important implications for  $\text{CO}_2$  capture and storage, oceanic and atmospheric carbon cycling, biomineralization, and oil and gas exploitations [1–5]. In industrial processes,  $\text{CaCO}_3$  is one of the most common mineral scales. When mineral water is widely used, undesirable scale formation is a major concern for energy production [5,6]. Such scaling phenomenon often leads to numerous technical and economic problems such as total or partial blockage of pipes resulting in a decrease in flow rate, reduction of heat transfer

efficiency, localized damage due to corrosion, failure in the structural metal, and unscheduled equipment shutdown [7–9]. For example, in power plants, the rate of power production is often limited by the scale formation in water-cooling systems, which can also be the origin of microbial proliferation [6]. In oil or gas production wells, mineral scaling reduces the overall fluid flow rate, causes formation or production damage in the reservoir, and thus poses a threat to safe production operations [10,11]. Quantitatively understanding the crystallization mechanism of the  $\text{CaCO}_3$  precipitation has gained a great interest. Therefore, it is relevant to know the influencing factors of scale formation and to control the scaling process, facilitating to prevent scale deposition.

Generally,  $\text{CaCO}_3$  crystallizes naturally in three polymorphs: calcite (rhombohedral, with a cubic shape), aragonite (orthorhombic, with needle and cauliflower shapes), and few vaterite (hexagonal, with a hexagonal shape), listed in an order of decreasing stability [12–14]. Calcite is thermodynamically stable at atmospheric pres-

\* Corresponding author at: Beijing Key Laboratory of Optical Detection Technology for Oil and Gas, College of Science, China University of Petroleum (Beijing), Beijing 102249, China.

\*\* Corresponding author.

E-mail addresses: [zilong@cup.edu.cn](mailto:zilong@cup.edu.cn) (Z. Liu), [lvqc@cup.edu.cn](mailto:lvqc@cup.edu.cn) (Q. Lv).

sure within the 0 – 90 °C temperature range [15], whereas vaterite is metastable and tends to transform into aragonite or calcite [16]. Depending on the experimental conditions, all three polymorphs can be obtained and calcite is more often the main constituent of CaCO<sub>3</sub> scales. Factors influencing the precipitation behavior of CaCO<sub>3</sub> on a metal surface include types of substrate [17], temperature [15], pH [18], foreign ionic or molecular species [19,20], organic additives [21,22], saturation level of water [23], electric fields [24], microorganisms [25], and electrochemical corrosion behavior at the metal-water interface [12,16,26]. To evaluate the deposition process, traditional methods consist in preparing a supersaturated liquid by mixing a solution of a soluble carbonate (e.g. Na<sub>2</sub>CO<sub>3</sub>, NaHCO<sub>3</sub>) with a solution of a soluble calcium salt (e.g. CaCl<sub>2</sub>) [13,14,27]. Precipitation of CaCO<sub>3</sub> can be achieved by removing dissolved CO<sub>2</sub> under moderate stirring, resulting in an increase of the solution pH, or adding salt ions resulting in a slight supersaturation [28,29]. However, this procedure is time consuming, and cannot monitor the CaCO<sub>3</sub> deposition in real-time and does not provide kinetic data. For this reason, a considerable interest was devoted to electrochemical techniques (chrono-electrogravimetry, impedance spectrometry and chronoamperometry) to investigate and accelerate calcareous precipitations [30].

Electrochemically induced deposition occurs on the electrode surface of a metallic substrate by increasing the interfacial pH caused by oxygen and water reduction reactions through applying a cathodic potential, and thus shifts the chemical equilibrium towards CaCO<sub>3</sub> precipitation [31,32]. This technique was further improved by a coupling quartz crystal microbalance with electrochemical techniques (EQCM) [33]. The EQCM allows *in situ*, fast and highly sensitive (nanogram level of generated CaCO<sub>3</sub>) mass change measurements of the scaling behavior. Using a transparent EQCM in an impinging jet cell, the rate of the CaCO<sub>3</sub> deposition increased with the convection until a limiting value of the Reynolds number was reached [34]. Amor et al. investigated the influence of the sulfate and magnesium ions on the nucleation-growth process of CaCO<sub>3</sub> electrodeposition [35,36]. Two kinds of poly(acrylic acid-co-maleic acid) and polyaspartic acid were reported to efficiently prevent the formation of CaCO<sub>3</sub>, depending on their concentrations [12]. Direct detection of calcium carbonate scaling was monitored on a pre-calcified sensitive electrode surface, showing a better sensitivity, especially for water in the presence of inhibitors, such as humic substances [27]. The inhibiting effect of Zn<sup>2+</sup> was demonstrated on the delay of calcium carbonate precipitation, even at very low concentration about 2 ppm [28]. Inserting EQCM in a channel flow cell, the inhibiting properties of a phosphonate on CaCO<sub>3</sub> precipitation was evaluated under liquid flow conditions [37]. A calcite model mineral surface was obtained by electrochemically assisted deposition, which was subsequently used to study the effect of Na<sup>+</sup> and Ca<sup>2+</sup> concentration on the anionic surfactant adsorption [32]. There are a small number of studies to evaluate the scaling processes *in situ* using EQCM, however, the kinetics and mechanisms of CaCO<sub>3</sub> depositions are not yet well understood.

Different to the usual EQCM setup [33,36,38], we used EQCM with dissipation monitoring (EQCM-D) which shows advantages of easily controlling the flow rate and changing the solution compositions [39]. In this work, we set out to study the electrochemically induced CaCO<sub>3</sub> depositions on Pt sensor surfaces in a three-electrode flow cell, and related the recorded changes in resonance frequencies to the mass change of the sensor. The use of EQCM-D in combination with scanning electron microscopy (SEM) facilitated in a better understanding of the deposition behavior, allowing for the comprehensive description of the mass, thickness, morphology, surface coverage, and deposition rate of electrocrystallized CaCO<sub>3</sub>. With various applied potentials, CaCO<sub>3</sub> precipitations were compared under the conditions of liquid flow and in the absence of flow. As much as a twice higher surface coverage (~ 60%) was ob-

tained in the absence of flow, compared to conditions with a liquid flow. Further, under no-flow conditions, an inflection point (IP) was defined where the change in deposition rate started to change sign. When increasing the concentration of HCO<sub>3</sub><sup>-</sup> and Ca<sup>2+</sup>, CaCO<sub>3</sub> deposition rate and mass increased correspondingly. Additionally, the inhibiting effect of Mg<sup>2+</sup> on the deposition kinetics of CaCO<sub>3</sub> was observed. A new interpretation is proposed to identify the effectiveness of inorganic inhibitor (Mg<sup>2+</sup>).

## 2. Experimental methods

### 2.1. Chemicals and QCM-D sensors

CaCl<sub>2</sub>·2H<sub>2</sub>O (147.01 g/mol, ≥ 99%), MgCl<sub>2</sub>·6H<sub>2</sub>O (203.30 g/mol, ≥ 99%), and NaHCO<sub>3</sub> (84.01 g/mol, ≥ 99.5%) were purchased from Sigma Aldrich. NaNO<sub>3</sub> (84.99 g/mol, ≥ 99.5%), HCl (1 M) and NaOH (1 M) were purchased from Merck. Ethanol (≥ 96%), isopropanol (≥ 98%) and centrifugal tubes (50 mL) were purchased from VWR International. All compounds were used as received without further purification. Whatman filter papers (11 μm pore size) were purchased from Fischer Scientific. All salt solutions were prepared by dissolving the appropriate amounts of solute in de-ionized water (Milli-Q, resistivity of > 18.2 MΩ·cm, and 5.3 ppb TOC). The used Pt (QS-QSX314) covered QCM-D sensors (diameter = 14 mm, thickness = 0.3 mm) were purchased from Q-Sense Biolin Scientific.

### 2.2. Electrochemically assisted CaCO<sub>3</sub> depositions

To evaluate electrochemically induced CaCO<sub>3</sub> depositions, Pt substrates acted as a cathode (negative electrode) in an aqueous solution containing Ca<sup>2+</sup> and HCO<sub>3</sub><sup>-</sup> ions. For this purpose, the Q-Sense QCM-D and Q-Sense Explorer electrochemistry module from Biolin Scientific were used. An Electrochemical Analyzer from CH Instruments (CHI600D) was coupled to a three-electrode flow cell. The Pt covered QCM-D sensor was mounted in the electrochemical cell module and served as the working electrode. A Pt counter electrode and Ag/AgCl (3 M KCl saturated) reference electrode were used. In- and out-flow of solutions through the flow module were modulated by a REGLO digital peristaltic pump from Ismatec. The PDC-002-CE plasma cleaner from Harrick Plasma and RET Basic magnetic stirrer from IKA were used to remove any possible contaminations from the surface of the used Pt sensors. All EQCM-D measurements were performed at room temperature in a supporting electrolyte containing an excess of nitrate. All potential difference values given in this study are quoted against Ag/AgCl (3 M KCl).

The CaCO<sub>3</sub> deposition solution was made by first preparing two precursor solutions, one containing Ca<sup>2+</sup> ions (CaCl<sub>2</sub> solution) and the other containing HCO<sub>3</sub><sup>-</sup> ions (NaHCO<sub>3</sub> solution), which have the same solution concentration. These solutions also contained 500 mM NaNO<sub>3</sub>, which acts as a background electrolyte and OH<sup>-</sup> supplier. The pH of these solutions was adjusted to 7 ± 0.1 with drops of diluted NaOH or HCl to minimize CaCO<sub>3</sub> precipitation upon mixing. Then, the solution containing HCO<sub>3</sub><sup>-</sup> ions was added to solution containing Ca<sup>2+</sup> ions in a dropwise manner while magnetically stirring at 1500 rpm in order to make the CaCO<sub>3</sub> deposition solution. The CaCO<sub>3</sub> deposition solution was filtered into a centrifugal tube to remove any precipitated CaCO<sub>3</sub>. Then, the cleaned QCM-D sensor was loaded into the flow module and all necessary connections (electrochemistry module and tubing from the pump) were connected.

Next, the pump was turned on and the measurement was started. Across all depositions, the CaCO<sub>3</sub> deposition solution was fed to the flow module for 10 min to establish a baseline frequency. Then, a negative voltage was applied in the potentiostatic mode (chronoamperometry) for 10 min. The frequency shift and

current flowing through the sensor/contacting solution interface were monitored as the deposition progressed. After the applied voltage was turned off, the sensor was left to equilibrate until a final, stable frequency signal had been reached. The resonance frequency was considered to be stable if the resonance frequency shift was less than 1% of the total resonance frequency shift over a 20 min period. Then, the deposited metal-CaCO<sub>3</sub> sensor was directly taken out of the flow module and placed on a petri dish, after which it was put in an oven set at a temperature of 60 °C to dry overnight.

### 2.3. Scanning electron microscopy experiments

A JSM-IT200 Intouchscope™ scanning electron microscope (SEM) from JEOL was used to study the morphology, surface coverage and chemical composition of the modified sensors. The morphology of the deposited Pt-CaCO<sub>3</sub> sensors was investigated using secondary electron image (SEI) mode. For all micrographs, an electron beam voltage of 5 kV was used. Generally, a spot size of 30 nm was used and micrograph images were taken at 50 – 2000 times magnification in the centre area of all sensors. SEM with energy dispersive X-ray analysis (SEM-EDX) was performed for elemental composition analyses in backscatter electron image (BEI) mode. An electron beam voltage of 20 kV was used and the spot size was adjusted such that a minimum of 5000 counts per second (cps) was reached on the detector. This ensured that the detector was sensitive enough to perform EDX measurements.

SEM images for coverage determination were taken in BEI mode. For this purpose, five different micrographs were taken: four different sites and the centre area. An example of a BEI image and an indication of the areas taken for coverage determination are shown in Figure S1. These images were mapped onto a binary black and white colour format using a Python script. The black regions of the image are the CaCO<sub>3</sub> deposit spots and the white parts consist of the clean Pt sensor surface. Then, the calculated relative occurrence of black and white pixels was taken as a measure for the sensor coverage.

### 2.4. QCM-D principle

The working principle behind a QCM-D is based on the converse piezoelectric effect. When an alternating voltage is applied, a shear stress is generated across a piezoelectric material, resulting in the oscillation of the material at its resonance frequency [40]. Quartz crystals are often used as the piezoelectric material because they vibrate with minimal energy dissipation, making them ideal oscillators [41]. Once a stable resonance frequency has been obtained, it can be perturbed by the adsorption (or desorption) of mass on (or from) the crystal surface. The linear relation between the change in mass ( $\Delta m$ ) and frequency shift ( $\Delta f$ ) can be described by the Sauerbrey equation [42].

$$\Delta f = -\frac{2nf_0^2\Delta m}{\rho_q v_q} = -\frac{n\Delta m}{C} \quad (1)$$

where  $f_0$  is the fundamental resonant frequency,  $n$  is the overtone number (1, 3, 5, etc.),  $\rho_q$  is the specific density of quartz (2650 kg m<sup>-3</sup>),  $v_q$  is the shear wave velocity (3340 m s<sup>-1</sup>), and  $C$  is the sensitivity constant of the quartz crystal (17.7 ng cm<sup>-2</sup> Hz<sup>-1</sup>). The Sauerbrey equation is suitable under the condition that the adsorbed film couples perfectly with the shear oscillation. In that case, the adsorbed layer is supposed to be rigid, thin, uniformly distributed, and does not slip at the interface [43,44]. In this work, the deposited CaCO<sub>3</sub> layer was regarded as a rigid layer and evenly distributed on the Pt surface. Besides, the dissipation change was relatively small compared to  $\Delta f$  (lower than 10<sup>-7</sup> Hz<sup>-1</sup>) for 5 MHz Pt sensors. As a result, the Sauerbrey model has been applied to

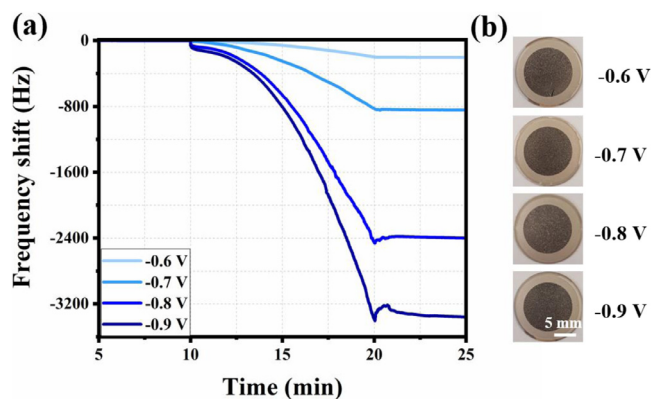


Fig. 1. (a) QCM-D frequency monitoring of CaCO<sub>3</sub> deposition processes on Pt sensors with different applied voltages. (b) Optical micrographs of the deposited CaCO<sub>3</sub> sensors.

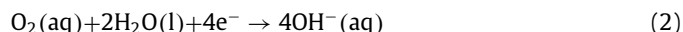
calculate the deposited mass and thickness of the CaCO<sub>3</sub> layer. It was found that the third harmonic of the fundamental resonance frequency resulted in a better signal-to-noise ratio and was therefore chosen for our measurements.

## 3. Results and discussions

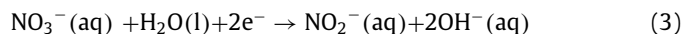
### 3.1. Effect of applied voltages

Before CaCO<sub>3</sub> depositions, the linear sweep voltammogram were performed to select the optimal reduction potentials that was further applied to the working electrode during chronoamperometrically and electrochemically assisted CaCO<sub>3</sub> deposition process. The cathodically polarized working electrode acts as cathode and underwent the electrogeneration of hydroxide ions at the electrode surface with following reduction reactions:

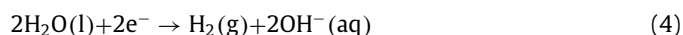
Oxygen reduction:



Nitrate reduction:



Water reduction:



To avoid the formation of hydrogen bubbles, we applied a voltage of -0.6, -0.7, -0.8, and -0.9 V with the EQCM-D to investigate the effect of the applied voltage on the deposition of CaCO<sub>3</sub>. For this purpose, a CaCO<sub>3</sub> deposition solution containing 50 mM CaCl<sub>2</sub>, 50 mM NaHCO<sub>3</sub>, and 500 mM NaNO<sub>3</sub> was fed to the flow module at a rate of 200  $\mu\text{L min}^{-1}$  for the first 10 min of measurement in order to obtain the baseline frequency. Then, the voltage was applied for another 10 min ( $t = 10$  to 20 min), after which the sensor was left to stabilize for the final 40 min of measurement. The results of this set of experiments are illustrated in Fig. 1a and the whole deposition period can be found in Figure S2a. At  $t = 10$  min the voltage is applied and the resonance frequency shifts to lower values. This is caused by a mass increase of the sensor because CaCO<sub>3</sub> is being deposited onto the sensor as the electrochemically assisted CaCO<sub>3</sub> deposition process progresses. Moreover, the applied voltage does have an important effect on the initial nucleation of CaCO<sub>3</sub> crystals (Figure S2b). The frequency shifts to an initial nucleation equilibrium in the first 30 to 60 s. After an initial short period of nucleation, the growth rate of the CaCO<sub>3</sub> crystals is accelerating until the applied voltage is stopped. When the applied voltage is turned off at  $t = 20$  min, the frequency remains stable. During this stabilization period from  $t = 20$  to 60 min, the

**Table 1**

The applied voltage, deposited mass, thickness, and surface coverage of deposited CaCO<sub>3</sub> sensors.

| <i>E</i> (V) | $\Delta m$ ( $\mu\text{g}$ ) | thickness (nm) | Coverage <sup>a</sup> (%) |
|--------------|------------------------------|----------------|---------------------------|
| -0.6         | 5.3 ± 0.4                    | 20 ± 1         | 28.0 ± 0.7                |
| -0.7         | 16.4 ± 1.2                   | 62 ± 5         | 31.6 ± 1.4                |
| -0.8         | 45.0 ± 2.1                   | 170 ± 8        | 34.8 ± 1.3                |
| -0.9         | 62.4 ± 3.3                   | 236 ± 13       | 35.8 ± 1.1                |

<sup>a</sup> Coverage is based on the SEM micrographics analysis.

CaCO<sub>3</sub> deposition solution is still flowing through the flow module. This observation suggests that the applied CaCO<sub>3</sub> coating is also stable and does not dissolve or detach due to the liquid flow. From the figure, it is also observed that a lower voltage results in a larger frequency shift. This is expected because applying a lower voltage results in a higher reduction current, which subsequently gives rise to more OH<sup>-</sup> generation and thus more CaCO<sub>3</sub> formation. The chronoamperometric curves of this set of measurement are shown in Figure S3. These I-t curves are monitored in tandem with the electrodeposition and provide information about the current density of the sensor as the deposition progresses. In general, a decreasing current is observed over time for all applied voltages as the forming CaCO<sub>3</sub> layer is insulating. This suggests a gradual increase of sensor coverage with CaCO<sub>3</sub>. As expected, this current density decreases fastest for a lower applied voltage because more CaCO<sub>3</sub> is being deposited in the same time period when lower voltages are applied.

In Fig. 1b, it shows the appearances of the deposited CaCO<sub>3</sub> sensors, indicating that CaCO<sub>3</sub> particles are deposited uniformly over the Pt substrate. Under the used experimental conditions, the applied voltage does not have significant visual differences on the physical appearance of the sensor. To characterize the deposited CaCO<sub>3</sub>, the deposited mass and thickness, as well as the surface coverage of the CaCO<sub>3</sub> sensors are summarized in Table 1. The deposited mass and coating thickness of CaCO<sub>3</sub> were calculated with the Sauerbrey model assuming a high rigidity of the deposited CaCO<sub>3</sub> (see Section 2.4). A lower applied voltage results in more deposition of CaCO<sub>3</sub> mass and an increased thickness, which are consistent with the observed larger frequency shift at the lower applied voltage. Also, the surface coverage is found to increase with decreasing applied voltages. However, this cannot be stated with certainty as the coverages of the sensors deposited with an applied voltage of -0.8 and -0.9 V are within their margin of error. Interestingly, it also suggests that the surface coverage does not change as much as the change in deposited mass for all applied voltages. It can be stated that after a certain point, the additional depositions of CaCO<sub>3</sub> are more likely to grow on top of the existing CaCO<sub>3</sub> crystals (thus, increasing the thickness) instead of being deposited over the whole sensor where it would also cause the surface coverage to increase more. Additionally, the growth of the crystals was often accompanied by Ostwald ripening. The larger crystals grow at the expense of dissolution of the smaller crystals [45], which would have a negative effect on the coverage due to the overall reduction of surface area to volume ratio.

The morphology of the deposited sensors is shown in Fig. 2. From the resulting SEM micrographs, it is observed that mostly cubic-like and rhombic-like CaCO<sub>3</sub> crystals were formed with sizes of around 25 – 40 μm. This suggests that the deposit was predominantly the mineral calcite rather than the thin needle-shaped aragonite, as calcite is thermodynamically most stable under ambient conditions. It can be further observed that the larger crystals were surrounded by regions of Pt surface, covered partly by smaller grains. This confirms our earlier description that by Ostwald ripening the larger crystals are preferred to form over smaller crystals. At -0.8 and -0.9 V, the formation of amorphous crystals

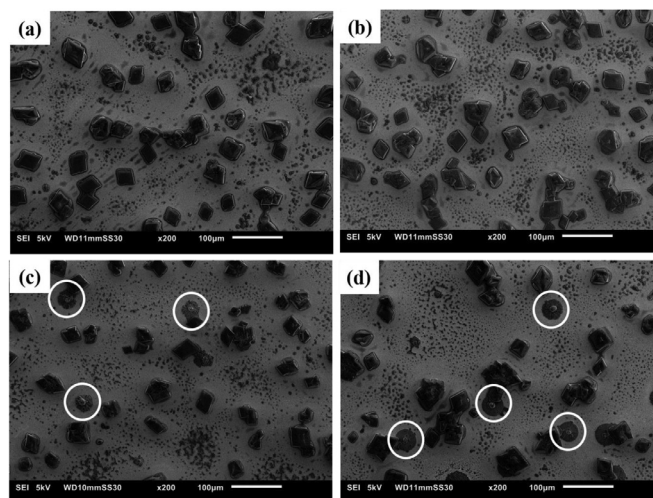


**Fig. 2.** SEM micrographs (200 times magnification) of the deposited sensors with an applied voltage of (a) -0.6 V, (b) -0.7 V, (c) -0.8 V, and (d) -0.9 V. The observed amorphous crystals are circled in white.

is observed, indicated with white circles in Fig. 2c and 2d. An explanation for this could be that a lower voltage generates a larger driving force for newly formed CaCO<sub>3</sub> crystals to attach strongly to the Pt surface, giving them less freedom to rearrange in their preferred orientation. These amorphous crystals might be clusters of smaller crystals which do not have the freedom to rearrange into the more commonly observed edge-shaped crystals. Higher magnification SEM micrographs of these types of amorphous, clustered crystals are given in Figure S4. Furthermore, an EDX analysis was performed on a SEM micrograph with both an edge-shaped and an amorphous CaCO<sub>3</sub> crystal (Figure S5). The atomic composition of the edge-shaped CaCO<sub>3</sub> crystal, normalized to calcium, was determined to be Ca: C: O = 1.0: 0.8: 2.5. Also, the atomic composition of the amorphous CaCO<sub>3</sub> crystal, normalized to calcium, was determined to be Ca: C: O = 1.0: 1.1: 3.1. The atomic compositions of these crystals confirm the chemical nature of the crystalline species to be calcium carbonate.

### 3.2. Effect of applied voltages in the absence of flow

The electrochemically assisted CaCO<sub>3</sub> precipitation was investigated in the absence of flow. Similar to Section 3.1, a CaCO<sub>3</sub> deposition solution containing 50 mM CaCl<sub>2</sub>, 50 mM NaHCO<sub>3</sub> and 500 mM NaNO<sub>3</sub> was flushed for the first 10 min to obtain the baseline frequency. Then, the flow was stopped, after which a voltage was applied for 30 min and the growth of CaCO<sub>3</sub> was monitored. The applied voltages were -0.6, -0.7, -0.8 and -0.9 V. After electrochemically assisted deposition, the frequency was left to stabilize for a period of more than 5 h. Fig. 3a shows the stable frequency change of this set of experiments during the first 50 min period. At that moment a potential is imposed (at *t* = 10 min), and the resonance frequency shifts to lower values as the electrocrystallization of CaCO<sub>3</sub> progresses. For lower applied voltages (-0.7, -0.8 and -0.9 V), a minimum value is reached in the resonance frequency. This is because, due to the absence of flow, at some point the sensor reaches its maximum loading of CaCO<sub>3</sub> as the precursor Ca<sup>2+</sup> and HCO<sub>3</sub><sup>-</sup> ions needed for CaCO<sub>3</sub> growth are consumed during the crystallization process. This behavior is not observed for an applied potential of -0.6 V because at this voltage an insufficient amounts of OH<sup>-</sup> are produced. It is also observed that the minimum frequency shift is related to the applied voltage. A lower applied voltage results in more initial nucleation of CaCO<sub>3</sub> crystals. Thus, a larger amount of initial nuclei created on the Pt

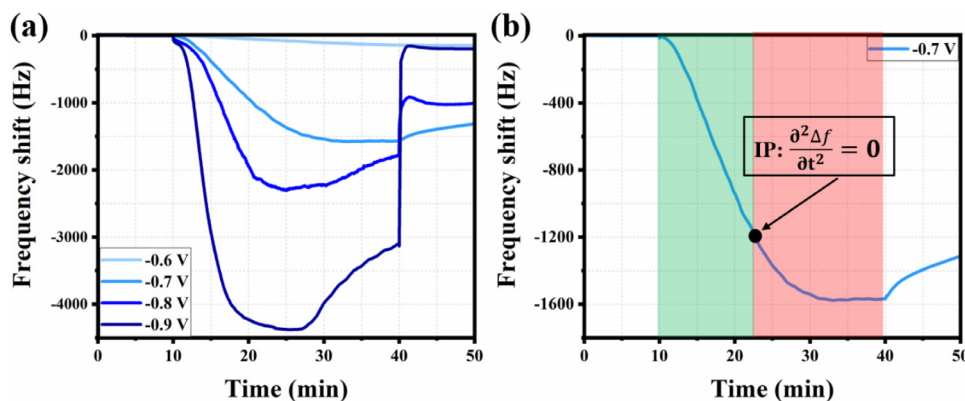


**Fig. 3.** (a) QCM-D frequency monitoring of  $\text{CaCO}_3$  deposition processes on Pt sensors with different applied voltages in the absence of flow. (b) Indication of the inflection point (IP) from a deposition graph monitored with QCM-D using an applied voltage of  $-0.7$  V in the absence of flow. Before the IP (green region), there is an excess concentration of  $\text{Ca}^{2+}$  and  $\text{HCO}_3^-$  ions present in the flow module and the deposition rate is accelerating. At the IP (black dot), the concentration of  $\text{Ca}^{2+}$  and  $\text{HCO}_3^-$  ions are in equilibrium with the  $\text{CaCO}_3$  growth rate. After the IP (red region), the concentration of  $\text{Ca}^{2+}$  and  $\text{HCO}_3^-$  ions is insufficient in maintaining accelerating growth and the  $\text{CaCO}_3$  growth rate is decelerating until the maximum deposited mass of  $\text{CaCO}_3$  is reached. (For interpretation of the references to colour in this figure legend, the reader is referred to the web version of this article.)

substrate in the beginning of the electrocrystallization process provide a better surface for more  $\text{CaCO}_3$  growth. After this minimum frequency is reached for these lower applied potentials, the voltage is still applied until  $t = 40$  min. A subsequent increase of frequency is observed for applied voltages of  $-0.8$  and  $-0.9$  V (starting at approximately  $t = 25$  min). This would mean that the  $\text{CaCO}_3$  coating is either dissolving or detaching from the Pt substrate as the sensor is losing mass. It is likely that, at these low applied voltages, the  $\text{CaCO}_3$  layer is detaching from the substrate as there is still a continuous generation of  $\text{OH}^-$  ions at the metal surface, between the Pt substrate and  $\text{CaCO}_3$  layer, due to the applied potential. This formation of  $\text{OH}^-$  ions is not being used for  $\text{CaCO}_3$  formation as the maximum loading has already been reached and can subsequently weaken the binding of the coating with the substrate and push it off the surface.

At  $t = 40$  min the applied voltage is stopped and a sudden, sharp increase in frequency is observed and this effect is found to be larger for lower applied voltages. To some extent, this effect resembles the stretching of a rubber band. Recall from the  $\text{CaCO}_3$  formation reactions that  $\text{HCO}_3^-$  reacts with  $\text{OH}^-$  to form  $\text{CaCO}_3$  and  $\text{H}_2\text{O}$ . Thus, a sudden stop in applied voltage may force the accumulated  $\text{OH}^-$  ions to repel from the anode of the sensor, which is registered as a sudden loss of mass by the QCM-D analyzer and thus a sharp increase in frequency is observed at that point. Besides, the shape of chronoamperometric curves (Figure S6) resembles the deposition graphs. It suggests that an excess amount of  $\text{OH}^-$  ions is created, which cannot contribute to more  $\text{CaCO}_3$  formation as the maximum amount of deposited mass of  $\text{CaCO}_3$  has already been reached.

An interesting observation that can be made from Fig. 3b is that the growth rate accelerates in the beginning and slows down later. The moment at which the growth rate switches from accelerating to decelerating is characterized by an inflection point (IP). At this point, the second derivative of the change of the measured frequency shift to the time is zero, defined as:

$$\frac{\partial^2 \Delta f}{\partial t^2} = 0 \quad (5)$$

Because there is no flow of  $\text{CaCO}_3$  deposition solution, there is no supply of  $\text{Ca}^{2+}$  and  $\text{HCO}_3^-$  ions, and this results in a decrease of their concentrations as the crystallization process progresses. Before the IP, the concentrations of  $\text{Ca}^{2+}$  and  $\text{HCO}_3^-$  are in excess and the growth of  $\text{CaCO}_3$  increases in time. After the IP, concentrations of  $\text{Ca}^{2+}$  and  $\text{HCO}_3^-$  are insufficient in maintaining the accelerating growth and limit the growth rate of  $\text{CaCO}_3$  deposition. The maxi-

**Table 2**

The applied voltage, maximum deposited  $\text{CaCO}_3$  mass, thickness, surface coverage, and IP of deposited  $\text{CaCO}_3$  sensors.

| $E$ (V) | $\Delta m$ ( $\mu\text{g}$ ) | thickness (nm) | Coverage <sup>a</sup> (%) | IP <sup>b</sup> (min) |
|---------|------------------------------|----------------|---------------------------|-----------------------|
| $-0.6$  | $2.1 \pm 0.1$                | $10 \pm 1$     | $36.6 \pm 1.6$            | -                     |
| $-0.7$  | $22.8 \pm 1.0$               | $110 \pm 5$    | $62.1 \pm 2.4$            | 13.2                  |
| $-0.8$  | $34.0 \pm 3.3$               | $160 \pm 16$   | $60.7 \pm 2.1$            | 6.7                   |
| $-0.9$  | $63.5 \pm 2.8$               | $305 \pm 14$   | $62.0 \pm 3.1$            | 2.5                   |

<sup>a</sup> Coverage is based on the SEM micrographics analysis.

<sup>b</sup> IP is determined by computing the time at which the second derivative of the polynomial was equal to zero with an equation solver.

imum amount of deposited  $\text{CaCO}_3$  mass, coating thickness, surface coverage, and IP of the produced  $\text{CaCO}_3$  sensors were calculated and are given in Table 2. The values of the IP shown in the table correspond to the time after the voltage was applied, e.g.: an IP of 13.2 min corresponds to 23.2 min in the deposition graphs shown in Fig. 3b. It can be observed that a lower applied voltage results in a lower IP. This means that applying a lower voltage results in a higher consumption rate of the present  $\text{Ca}^{2+}$  and  $\text{HCO}_3^-$  ions. This is expected because a lower applied voltage results in a higher rate of  $\text{OH}^-$  production and thus a higher consumption rate of  $\text{Ca}^{2+}$  and  $\text{HCO}_3^-$  ions. An IP is not observed for an applied voltage of  $-0.6$  V because, for the time during the voltage is applied, the consumption rate of  $\text{Ca}^{2+}$  and  $\text{HCO}_3^-$  ions is too low to reach an IP.

The applied voltage is also closely related to the maximum deposited mass: a lower applied voltage results in a higher maximum amount of  $\text{CaCO}_3$  deposition. For an applied voltage of  $-0.6$  V, it is significantly lower than observed for the other applied voltages. The reason for this is that, by applying a voltage of  $-0.6$  V, a "maximum amount of deposited mass" is not reached (within the time frame of applying the voltage) because the reduction current and  $\text{OH}^-$  production is too low to achieve a maximum amount of deposited mass. It is remarkable that depositing  $\text{CaCO}_3$  in the absence of flow results in much higher surface coverages (in the order of 60%) as compared to carrying out the deposition at a flow rate of  $200 \mu\text{L min}^{-1}$  (in the order of 30%, as shown in Table 1). This can be attributed to the fact that the formed  $\text{CaCO}_3$  nuclei have a higher probability of staying attached on the Pt substrate surface under no flow conditions, resulting in higher surface coverages. The main characteristic of the morphology of the precipitated  $\text{CaCO}_3$  surface is that thin layers surrounding the edge-shaped  $\text{CaCO}_3$  crystals can be observed in Figure S7. These layers were most likely formed after a maximum amount of deposited

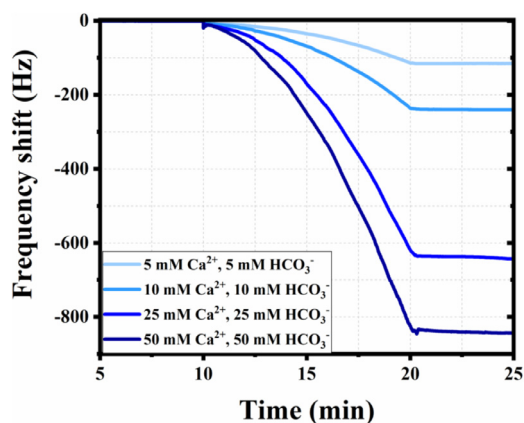


**Fig. 4.** QCM-D frequency monitoring of  $\text{CaCO}_3$  deposition processes on Pt sensors with different  $\text{Ca}^{2+}$  and  $\text{HCO}_3^-$  concentrations of 5, 10, 25 and 50 mM. A constant applied voltage of  $-0.7$  V and a flow rate of  $200 \mu\text{L min}^{-1}$  were applied.

**Table 3**

The deposition mass, thickness and surface coverage of the deposited  $\text{CaCO}_3$  sensors with different  $\text{Ca}^{2+}$  and  $\text{HCO}_3^-$  concentrations.

| $[\text{Ca}^{2+}]$ and $[\text{HCO}_3^-]$ (mM) | $\Delta m$ ( $\mu\text{g}$ ) | thickness (nm) | Coverage <sup>a</sup> (%) |
|--|------------------------------|----------------|---------------------------|
| 5  | $1.7 \pm 0.2$                | $9 \pm 1$      | $17.2 \pm 2.7$            |
| 10   | $3.5 \pm 0.2$                | $17 \pm 1$     | $24.0 \pm 1.6$            |
| 25   | $9.4 \pm 0.7$                | $45 \pm 3$     | $32.1 \pm 1.4$            |
| 50   | $12.9 \pm 0.9$               | $62 \pm 5$     | $31.6 \pm 1.4$            |

<sup>a</sup> Coverage is based on the SEM micrographics analysis.

mass was reached. Also, in the absence of flow these thin layers were not flushed away, but remained on the surface of the sensor, which is likely the reason that these thin layers are not seen on  $\text{CaCO}_3$  sensors deposited under flow conditions.

### 3.3. Effect of $\text{Ca}^{2+}$ and $\text{HCO}_3^-$ concentrations

In this section, we investigated the  $\text{CaCO}_3$  deposition with solutions containing  $\text{Ca}^{2+}$  and  $\text{HCO}_3^-$  concentrations of 5, 10, 25 and 50 mM, together with 500 mM  $\text{NaNO}_3$ . A constant applied voltage of  $-0.7$  V and a flow rate of  $200 \mu\text{L min}^{-1}$  was used. The first 10 min of experiments were used to establish the baseline frequency. Then, the chosen voltage was applied for 10 min, after which the frequency was let to equilibrate for the final 40 min of the measurement. Fig. 4 shows the frequency change as monitored with the QCM-D until a stable signal is reached. It can be observed that the deposited mass of  $\text{CaCO}_3$  is related to the precursor  $\text{Ca}^{2+}$  and  $\text{HCO}_3^-$  concentrations fed to the flow module. Lower  $\text{CaCO}_3$  precursor concentrations lead to a lower amount of deposited  $\text{CaCO}_3$  mass. A proportional relation can be observed when comparing precursor concentrations of 5, 10 and 25 mM  $\text{Ca}^{2+}$  and  $\text{HCO}_3^-$  to the frequency shift. The used concentration ratio of 5 mM: 10 mM: 25 mM is roughly equal to the resulting frequency shift ratio of 117 Hz: 225 Hz: 651 Hz. However, this relation cannot be extended to a precursor concentration of 50 mM as the resulting frequency shift of this concentration is found to be 875 Hz. This suggests that there is an upper limit of the precursor concentration that can be used to deposit as much  $\text{CaCO}_3$  mass as possible, under the used experimental conditions.

The mass deposited and the layer thickness, together with the obtained sensor surface coverages of the made  $\text{CaCO}_3$  sensors under varying precursor concentrations conditions are shown in Table 3. From this table it can be observed that both the electrocrystallized  $\text{CaCO}_3$  mass and coating thickness increased with increasing precursor  $\text{Ca}^{2+}$  and  $\text{HCO}_3^-$  concentrations. As was discussed, there was no linear relation between the used precursor

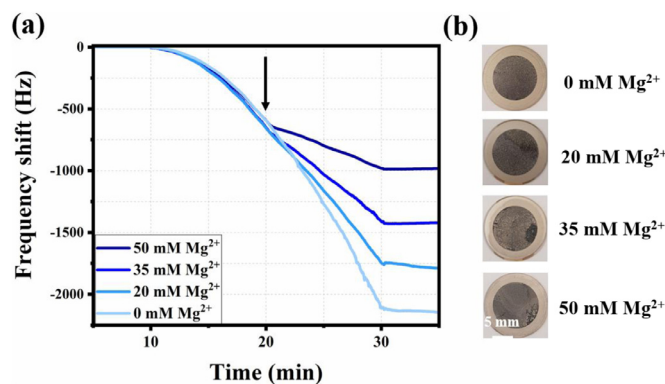


**Fig. 5.** (a) QCM-D frequency monitoring of  $\text{CaCO}_3$  deposition processes on Pt sensors in the presence and absence of  $\text{Mg}^{2+}$ . The black arrow indicates the times of injecting with the  $\text{MgCl}_2$  solution. (b) Optical micrographs of the deposited  $\text{CaCO}_3$  sensors.

concentration and the deposited mass. The surface coverages of the  $\text{CaCO}_3$  deposited sensor with precursor concentrations of 5 and 10 mM are lower than the sensors deposited with precursor concentrations of 25 and 50 mM. However, the surface coverage of the  $\text{CaCO}_3$  deposited sensor with a precursor concentration of 25 mM is more or less the same as the sensor produced with a precursor concentration of 50 mM. Looking into the SEM micrographs (Figure S8), the overall  $\text{CaCO}_3$  crystal sizes with precursor concentrations of 5 and 10 mM appear smaller than the crystal sizes with the higher precursor concentrations. A smaller precursor concentration results in a smaller production of initial amount of  $\text{CaCO}_3$  nuclei, which in turn results in smaller  $\text{CaCO}_3$  clusters that do not grow as large as when a higher precursor concentration would have been used.

### 3.4. Inhibition effect of $\text{Mg}^{2+}$

In order to investigate the inhibition of  $\text{CaCO}_3$  scaling, electrochemical deposition of  $\text{CaCO}_3$  was carried out in the presence of  $\text{Mg}^{2+}$  ions. For this purpose,  $\text{MgCl}_2$  was chosen as the source of  $\text{Mg}^{2+}$  ions. First, a regular deposition solution containing 50 mM  $\text{CaCl}_2$ , 50 mM  $\text{NaHCO}_3$ , and 500 mM  $\text{NaNO}_3$  was fed to the flow module at  $200 \mu\text{L min}^{-1}$  for 10 min to obtain the baseline frequency. Then, a voltage of  $-0.7$  V was applied for 10 min with the regular deposition solution. Subsequently, the inlet tube was changed to a vial containing the regular deposition solution with a certain concentration of  $\text{Mg}^{2+}$  ions for another 10 min. The final 30 min of the measurement were used to let the frequency stabilize. Fig. 5a shows the real-time monitoring of electrochemically induced  $\text{CaCO}_3$  precipitations in the presence of  $\text{Mg}^{2+}$  ions. At  $t = 10$  to 20 min, all deposition experiments were carried out with the regular  $\text{CaCO}_3$  deposition solution containing no  $\text{Mg}^{2+}$  ions as a reference. At  $t = 20$  to 30 min, the injected solution was changed via a vial to a solution containing the  $\text{CaCO}_3$  deposition solution with chosen  $\text{Mg}^{2+}$  concentrations. It is observed that the deposition graphs of the sensors produced in the presence of  $\text{Mg}^{2+}$  begin to divert as compared to the deposition graph of the sensor carried out with the regular  $\text{CaCO}_3$  deposition solution. This indicates that the growth of  $\text{CaCO}_3$  is inhibited by the presence of  $\text{Mg}^{2+}$  ions. This inhibition causes the growth rate to reduce as the rate of the deposition changes from an "accelerating growth" to a "linear-like growth". It is also suggested that this reduction of growth rate is related to the concentration of  $\text{Mg}^{2+}$  ions: a higher concentration of  $\text{Mg}^{2+}$  present in the deposition solution causes a greater growth rate reduction. Fig. 5b illustrates the appearances of the sensors deposited in the presence of  $\text{Mg}^{2+}$ . The appearances of the formed  $\text{CaCO}_3$  coatings deposited in the presence of  $\text{Mg}^{2+}$  ions are

**Table 4**

The mass deposition, thickness, surface coverage and deposition rate reduction of the deposited CaCO<sub>3</sub> sensors in the presence of different Mg<sup>2+</sup> concentrations.

| [Mg <sup>2+</sup> ] (mM) | Δ <i>m</i> (μg) | thickness (nm) | Coverage <sup>a</sup> (%) | Deposition rate reduction <sup>b</sup> (min) |
|--------------------------|-----------------|----------------|---------------------------|--|
| 0                        | 43.5 ± 3.3      | 164 ± 12       | 37.1 ± 1.5                | 0  |
| 20                       | 35.2 ± 2.6      | 133 ± 10       | 29.5 ± 3.6                | 15   |
| 35                       | 28.0 ± 2.1      | 106 ± 8        | 31.2 ± 5.4                | 40   |
| 50                       | 19.2 ± 1.4      | 72 ± 5         | 31.9 ± 3.0                | 73   |

<sup>a</sup> Coverage is based on the SEM micrographics analysis.

<sup>b</sup> Deposition reduction rate is determined by comparing with the CaCO<sub>3</sub> growth rate before and after injecting Mg<sup>2+</sup> containing solution.

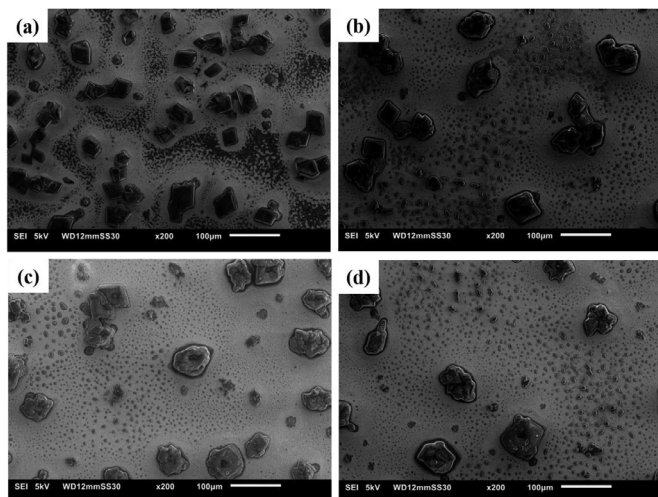


**Fig. 6.** SEM micrographs (200 times magnification) of the deposited sensors with a CaCO<sub>3</sub> deposition solution containing (a) 0 mM Mg<sup>2+</sup>, (b) 20 mM Mg<sup>2+</sup>, (c) 35 mM Mg<sup>2+</sup>, and (d) 50 mM Mg<sup>2+</sup>.

less uniform. This is especially the case for the coatings deposited in the presence of 35 and 50 mM Mg<sup>2+</sup>. For these deposited layers, there are larger uncoated regions on the sensor surface, which were likely caused by the higher concentrations of Mg<sup>2+</sup> present during the deposition process.

The deposited mass and thickness, together with the obtained sensor surface coverages and deposition rate reductions are shown in Table 4. It can be found that the deposited mass and thickness of the deposited CaCO<sub>3</sub> layer is lower as the concentration of the present Mg<sup>2+</sup> ions is higher. The surface coverage of the CaCO<sub>3</sub> deposited sensors without the presence of Mg<sup>2+</sup> is higher than the surface coverages of the sensors produced in the presence of Mg<sup>2+</sup>. This observation is in agreement with the appearances of the produced CaCO<sub>3</sub> sensors because the sensors produced in the presence of Mg<sup>2+</sup> appeared to have uncoated regions on the sensors (Fig. 5b). There is a positive relation between the present amount of Mg<sup>2+</sup> and the reduction of deposition rate. With the increase of Mg<sup>2+</sup> concentration, the reduction of deposition rate increases correspondingly, concluding that less deposited CaCO<sub>3</sub> is formed.

From the SEM micrographs (Fig. 6), the CaCO<sub>3</sub> precipitated surfaces in the presence of Mg<sup>2+</sup> (Fig. 6b-d) appear to have a substantial amount of very small crystals with sizes in the order of a few μm. It is suggested that the growth of these smaller crystals was likely suppressed by the incorporation of Mg<sup>2+</sup> into the crystal surface, preventing them from growing further into larger crystals. Also, there exists a distribution of crystal sizes as a function of the distance from the observed larger crystals. It can be ascribed to the Ostwald ripening process, as we discussed previously in Section 3.1. Furthermore, there are less cubic-shaped or edge-shaped CaCO<sub>3</sub> crystals in comparison with the crystals formed in the absence of Mg<sup>2+</sup>. It is likely that the incorporation of Mg<sup>2+</sup> into the crystal lattice of CaCO<sub>3</sub> disrupts the morphology of the

formed lattice. This was confirmed by EDX analysis of a CaCO<sub>3</sub> sensor that was deposited in the presence of 50 mM Mg<sup>2+</sup> (Figure S9). The relative atomic percentages of Ca, and Mg were 16.2%, and 1.2%, respectively. Assuming that all the Mg content found in the performed EDX analysis occupied a Ca lattice site, it is suggested that 6.7% of the Ca<sup>2+</sup> binding sites were occupied by Mg<sup>2+</sup>. Our observation is also well consistent with the results of Nielsen et al. [46], who concluded that a tiny amount of Mg<sup>2+</sup> adsorbed to CaCO<sub>3</sub> surfaces and can be incorporated into the growing mineral to block growth sites. The incorporation of Mg<sup>2+</sup> into the CaCO<sub>3</sub> mineral lattice also changes the energy landscape of the surface such that the adsorption energy of Ca<sup>2+</sup> also changed [3]. Only small changes in adsorption energy are required for large changes in CaCO<sub>3</sub> growth rate. The presence of Mg<sup>2+</sup> in the vicinity of Ca<sup>2+</sup> may result in a competition of which of these ions gets incorporated in the crystal surface first. Due to the smaller ionic radius of Mg<sup>2+</sup> ions as compared to Ca<sup>2+</sup> ions, Mg<sup>2+</sup> ions can diffuse faster into the crystal lattice and bind to a lattice site where normally a Ca<sup>2+</sup> ion would reside, thereby reducing further growth of CaCO<sub>3</sub> near that lattice site. In this case, the presence of Mg<sup>2+</sup> ions plays a significant role in inhibiting the CaCO<sub>3</sub> growth.

#### 4. Conclusions

Coupling of electrochemical techniques and QCM-D in one analysis setup (EQCM-D) opens up a new avenue to investigate the electrochemically induced CaCO<sub>3</sub> depositions under liquid flow conditions. We firstly studied the effect of applied voltages on the precipitation of CaCO<sub>3</sub> by applying a series of different voltages. A lower applied voltage resulted in more deposition of CaCO<sub>3</sub> mass and thickness, which were consistent with the observed larger frequency shift at the lower applied voltage. Also, CaCO<sub>3</sub> coverages in the order of 30% were found to increase with decreasing applied voltages. From the SEM micrographs, the CaCO<sub>3</sub> crystals were mostly cubic-like and rhombic-like with sizes of around 25 – 40 μm, which further grew due to Ostwald ripening. In the absence of flow, much higher CaCO<sub>3</sub> coverages in the order of 60% were obtained as compared to the deposition carried out with a flow rate of 200 μL min<sup>-1</sup>. The point at which the CaCO<sub>3</sub> growth rate switched from accelerating to decelerating is characterized by an inflection point (IP). A lower applied voltage resulted in a lower IP. This means that applying a lower voltage gave rise to a higher consumption rate of the present Ca<sup>2+</sup> and HCO<sub>3</sub><sup>-</sup> ions under no-flow conditions. The applied voltage was also closely related to the maximum deposited mass and thickness: a lower applied voltage resulted in more maximum CaCO<sub>3</sub> deposition.

Increasing precursor Ca<sup>2+</sup> and HCO<sub>3</sub><sup>-</sup> concentrations, both the electrocrystallized CaCO<sub>3</sub> mass and coating thickness increased correspondingly. In the investigation of the inhibition effect of Mg<sup>2+</sup> on CaCO<sub>3</sub> precipitation, a positive relation was found between the Mg<sup>2+</sup> concentration and deposition rate reduction, where the growth inhibition was more profound with increasing Mg<sup>2+</sup> concentration. A reduction in the growth rate of CaCO<sub>3</sub> as high as 73% was achieved in the presence of 50 mM Mg<sup>2+</sup>. The

inhibition effect of  $Mg^{2+}$  was explained by its incorporation into the growing minerals to block  $CaCO_3$  growth sites and suppress the smaller crystals to grow into bigger ones. These results provide new insight in the scaling process of  $CaCO_3$  and the formation of different scale morphologies under different conditions. Also, this study contributes to a better understanding of electrochemically induced  $CaCO_3$  depositions and underlines the importance to facilitate screen various experimental parameters, which is very useful to study industry scaling and anti-scaling processes.

### Declaration of Competing Interest

The authors declare no competing financial interest.

### Credit authorship contribution statement

**Zilong Liu:** Conceptualization, Data curation, Formal analysis, Investigation, Methodology, Supervision, Validation, Writing - original draft. **Hayati Onay:** Conceptualization, Data curation, Formal analysis, Investigation, Methodology, Validation. **Fengzhi Guo:** Investigation, Data curation, Formal analysis, Methodology. **Qichao Lv:** Formal analysis, Investigation, Writing - review & editing. **Ernst J.R. Sudhölter:** Conceptualization, Formal analysis, Funding acquisition, Project administration, Resources, Supervision, Writing - review & editing.

### Acknowledgments

The authors thank Dr. Mark Brewer, Dr. John van Wunnik, and Dr. Dirk Groenendijk (Shell Global Solutions, Amsterdam, The Netherlands) for their active discussions and careful corrections. The authors also thank Dr. Beien Wang of TU Delft for assisting in the calculation of the surface coverage of the deposited  $CaCO_3$  sensors. Technical assistance from Mr. Duco Bosma of TU Delft is highly appreciated. This work was supported by the Shell Global Solutions and Science Foundation of China University of Petroleum, Beijing (no. 2462020BJRC007).

### Supplementary materials

Supplementary material associated with this article can be found, in the online version, at [doi:10.1016/j.electacta.2021.137719](https://doi.org/10.1016/j.electacta.2021.137719).

### References

- [1] V. Nikulshina, C. Gebald, A. Steinfeld,  $CO_2$  capture from atmospheric air via consecutive CaO-carbonation and  $CaCO_3$ -calcination cycles in a fluidized-bed solar reactor, *Chem. Eng. J.* 146 (2) (2009) 244–248.
- [2] W.R. Howard, W.L. Prell, Late quaternary  $CaCO_3$  production and preservation in the southern ocean: implications for oceanic and atmospheric carbon cycling, *Paleoceanography* 9 (3) (1994) 453–482.
- [3] S. Dobberschütz, M.R. Nielsen, K.K. Sand, R. Civioc, N. Bovet, S.L.S. Stipp, M.P. Andersson, The mechanisms of crystal growth inhibition by organic and inorganic inhibitors, *Nat. Commun.* 9 (1) (2018) 1–6.
- [4] J. Li, M. Tang, Z. Ye, L. Chen, Y. Zhou, Scale formation and control in oil and gas fields: a review, *J. Dispers. Sci. Technol.* 38 (5) (2017) 661–670.
- [5] M. Chaussemier, E. Pourmohammash, D. Gelus, N. Pécoul, H. Perrot, J. Lédion, H. Cheap-Charpentier, O. Horner, State of art of natural inhibitors of calcium carbonate scaling. A review article, *Desalination* 356 (2015) 47–55.
- [6] A. Dirany, P. Drogui, M.A. El Khakani, Clean electrochemical deposition of calcium carbonate to prevent scale formation in cooling water systems, *Environ. Chem. Lett.* 14 (4) (2016) 507–514.
- [7] M.A. Kelland, Effect of various cations on the formation of calcium carbonate and barium sulfate scale with and without scale inhibitors, *Ind. Eng. Chem. Res.* 50 (9) (2011) 5852–5861.
- [8] T. Zhu, L. Wang, W. Sun, M. Wang, Z. Yang, T. Ji, S. Wang, Y. Wang, L. Xia, G. Liu, Origin of aragonite scale deposition on carbon steel at ambient circumstances, *Ind. Eng. Chem. Res.* 57 (1) (2018) 401–413.
- [9] M. Mpelwa, S.-F. Tang, State of the art of synthetic threshold scale inhibitors for mineral scaling in the petroleum industry: a review, *Pet. Sci.* (2019) 1–20.
- [10] N. Kohler, G. Courbin, F. Ropital, Static and dynamic evaluation of calcium carbonate scale formation and inhibition, in: *Proceedings of the SPE European Formation Damage Conference, Society of Petroleum Engineers*, 2001.
- [11] M.S. Kamal, I. Hussein, M. Mahmoud, A.S. Sultan, M.A. Saad, Oilfield scale formation and chemical removal: a review, *J. Pet. Sci. Eng.* 171 (2018) 127–139.
- [12] D. Peronno, H. Cheap-Charpentier, O. Horner, H. Perrot, Study of the inhibition effect of two polymers on calcium carbonate formation by fast controlled precipitation method and quartz crystal microbalance, *J. Water Process Eng.* 7 (2015) 11–20.
- [13] R. Sabzi, R. Arefinia, Investigation of zinc as a scale and corrosion inhibitor of carbon steel in artificial seawater, *Corros. Sci.* 153 (2019) 292–300.
- [14] C. Gabrielli, G. Maurin, G. Poindessous, R. Rosset, Nucleation and growth of calcium carbonate by an electrochemical scaling process, *J. Cryst. Growth* 200 (1–2) (1999) 236–250.
- [15] L.N. Plummer, E. Busenberg, The solubilities of calcite, aragonite and vaterite in  $CO_2$ - $H_2O$  solutions between 0 and 90 °C, and an evaluation of the aqueous model for the system  $CaCO_3$ - $CO_2$ - $H_2O$ , *Geochim. Cosmochim. Acta* 46 (6) (1982) 1011–1040.
- [16] C. Gabrielli, R. Jaouhari, S. Joiret, G. Maurin, P. Rousseau, Study of the electrochemical deposition of  $CaCO_3$  by in situ Raman spectroscopy I. Influence of the substrate, *J. Electrochem. Soc.* 150 (7) (2003) C478–C484.
- [17] K. Palanisamy, K. Sanjiv Raj, S. Bhuvaneshwari, V.K. Subramanian, A novel phenomenon of effect of metal on calcium carbonate scale, morphology, polymorphism and its deposition, *Mater. Res. Innov.* 21 (5) (2017) 294–303.
- [18] M.M. Tlili, M. Benamor, C. Gabrielli, H. Perrot, B. Tribollet, Influence of the interfacial pH on electrochemical  $CaCO_3$  precipitation, *J. Electrochem. Soc.* 150 (11) (2003) C765–C771.
- [19] Y.B. Amor, L. Bousselmi, B. Tribollet, E. Triki, Study of the effect of magnesium concentration on the deposit of allotropic forms of calcium carbonate and related carbon steel interface behavior, *Electrochim. Acta* 55 (16) (2010) 4820–4826.
- [20] T. Zhu, L. Wang, W. Sun, M. Wang, J. Tian, Z. Yang, S. Wang, L. Xia, S. He, Y. Zhou, The role of corrosion inhibition in the mitigation of  $CaCO_3$  scaling on steel surface, *Corros. Sci.* 140 (2018) 182–195.
- [21] Z. Belarbi, B. Sotta, L. Makhloufi, B. Tribollet, J. Gamby, Modelling of delay effect of calcium carbonate deposition kinetics on rotating disk electrode in the presence of green inhibitor, *Electrochim. Acta* 189 (2016) 118–127.
- [22] S. Polat, Evaluation of the effects of sodium laurate on calcium carbonate precipitation: characterization and optimization studies, *J. Cryst. Growth* 508 (2019) 8–18.
- [23] B. Cao, A.G. Stack, C.I. Steefel, D.J. DePaolo, L.N. Lammers, Y. Hu, Investigating calcite growth rates using a quartz crystal microbalance with dissipation (QCM-D), *Geochim. Cosmochim. Acta* 222 (2018) 269–283.
- [24] Y.I. Cho, C. Fan, B.-G. Choi, Theory of electronic anti-fouling technology to control precipitation fouling in heat exchangers, *Int. Commun. Heat Mass Transf.* 24 (6) (1997) 757–770.
- [25] S. Stocks-Fischer, J.K. Galinat, S.S. Bang, Microbiological precipitation of  $CaCO_3$ , *Soil Biol. Biochem.* 31 (11) (1999) 1563–1571.
- [26] D. Zhang, Q. Lin, N. Xue, P. Zhu, Z. Wang, Q. Ji, L. Dong, K. Yan, J. Wu, The kinetics, thermodynamics and mineral crystallography of  $CaCO_3$  precipitation by dissolved organic matter and salinity, *Sci. Total Environ.* 673 (2019) 546–552.
- [27] Y. Chao, O. Horner, F. Hui, J. Lédion, H. Perrot, Direct detection of calcium carbonate scaling via a pre-calcified sensitive area of a quartz crystal microbalance, *Desalination* 352 (2014) 103–108.
- [28] S. Benslimane, H. Perrot, R. Bennezar, K.-E. Bouhidel, Thermodynamic study of  $Zn^{2+}$  inhibition properties and mechanism on calcium carbonate precipitation by chemical and electrochemical methods, *Desalination* 398 (2016) 114–120.
- [29] J. Lédion, B. François, J. Vienne, Characterisation of the scaling properties of water by fast controlled precipitation test, *J. Eur. Hydrol.* 28 (1997) 15–36.
- [30] M. Piri, R. Arefinia, Investigation of the hydrogen evolution phenomenon on  $CaCO_3$  precipitation in artificial seawater, *Desalination* 444 (2018) 142–150.
- [31] R. Ketrane, B. Saidani, O. Gil, L. Leleyter, F. Baraud, Efficiency of five scale inhibitors on calcium carbonate precipitation from hard water: effect of temperature and concentration, *Desalination* 249 (3) (2009) 1397–1404.
- [32] R.M. Haaring, N. Kumar, D. Bosma, L. Poltorak, E.J. Sudholter, Electrochemically-assisted deposition of calcite for application in surfactant adsorption studies, *Energy Fuels* (2019).
- [33] C. Gabrielli, M. Keddad, A. Khalil, G. Maurin, H. Perrot, R. Rosset, M. Zidoune, Quartz crystal microbalance investigation of electrochemical calcium carbonate scaling, *J. Electrochem. Soc.* 145 (7) (1998) 2386.
- [34] O. Devos, C. Gabrielli, B. Tribollet, Nucleation-growth process of scale electrodeposition—influence of the mass transport, *Electrochim. Acta* 52 (1) (2006) 285–291.
- [35] Y.B. Amor, L. Bousselmi, M.-C. Bernard, B. Tribollet, Nucleation-growth process of calcium carbonate electrodeposition in artificial water—influence of the sulfate ions, *J. Cryst. Growth* 320 (1) (2011) 69–77.
- [36] O. Devos, S. Jakab, C. Gabrielli, S. Joiret, B. Tribollet, S. Picart, Nucleation-growth process of scale electrodeposition—influence of the magnesium ions, *J. Cryst. Growth* 311 (18) (2009) 4334–4342.
- [37] C. Garcia, G. Courbin, F. Ropital, C. Fiaud, Study of the scale inhibition by HEDP in a channel flow cell using a quartz crystal microbalance, *Electrochim. Acta* 46 (7) (2001) 973–985.
- [38] J. Tang, D. Cao, Y. Wang, C. Mohamad, L. Chen, H. Wang, Research on growth behavior of calcium carbonate scale by electrochemical quartz crystal microbalance, *Int. J. Electrochem. Sci.* 12 (2017) 11955–11971.
- [39] X. Quan, A. Heiskanen, M. Tenje, A. Boisen, In-situ monitoring of potential enhanced DNA related processes using electrochemical quartz crystal microbalance with dissipation (EQCM-D), *Electrochem. Commun.* 48 (2014) 111–114.

- [40] Z. Liu, P. Hedayati, M.K. Ghatkesar, W. Sun, H. Onay, D. Groenendijk, J. van Wunnik, E.J. Sudhölter, Reducing anionic surfactant adsorption using polyacrylate as sacrificial agent investigated by QCM-D, *J. Colloid Interface Sci.* 585 (2021) 1–11.
- [41] M.D. Ward, D.A. Buttry, In situ interfacial mass detection with piezoelectric transducers, *Science* 249 (4972) (1990) 1000–1007.
- [42] G. Sauerbrey, Verwendung von Schwingquarzen Zur Wägung Dünner Schichten Und Zur Mikrowägung, *Z. Für Phys.* 155 (2) (1959) 206–222.
- [43] Z. Liu, P. Hedayati, E.J. Sudhölter, R. Haaring, A.R. Shaik, N. Kumar, Adsorption behavior of anionic surfactants to silica surfaces in the presence of calcium ion and polystyrene sulfonate, *Colloids Surf. Physicochem. Eng. Asp.* (2020) 125074.
- [44] Z. Liu, M.K. Ghatkesar, E.J. Sudholter, B. Singh, N. Kumar, Understanding the cation dependent surfactant adsorption on clay minerals in oil recovery, *Energy Fuels* 33 (12) (2019) 12319–12329.
- [45] P.W. Voorhees, The theory of Ostwald ripening, *J. Stat. Phys.* 38 (1–2) (1985) 231–252.
- [46] M.R. Nielsen, K.K. Sand, J.D. Rodriguez-Blanco, N. Bovet, J. Generosi, K.N. Dalby, S.L.S Stipp, Inhibition of calcite growth: combined effects of  $Mg^{2+}$  and  $SO_4^{2-}$ , *Cryst. Growth Des.* 16 (11) (2016) 6199–6207.